k-space propagation models for acoustically heterogeneous media: Application to biomedical photoacoustics

B. T. Cox[a] and S. Kara
Department of Medical Physics and Bioengineering, University College London, Gower Street, London WC1E 6BT, United Kingdom

S. R. Arridge
Department of Computer Science, University College London, Gower Street, London WC1E 6BT, United Kingdom

P. C. Beard
Department of Medical Physics and Bioengineering, University College London, Gower Street, London WC1E 6BT, United Kingdom

(Received 29 September 2006; revised 22 February 2007; accepted 22 February 2007)

Biomedical applications of photoacoustics, in particular photoacoustic tomography, require efficient models of photoacoustic propagation that can incorporate realistic properties of soft tissue, such as acoustic inhomogeneities both for purposes of simulation and for use in model-based image reconstruction methods. *k*-space methods are well suited to modeling high-frequency acoustics applications as they require fewer mesh points per wavelength than conventional finite element and finite difference models, and larger time steps can be taken without a loss of stability or accuracy. They are also straighforward to encode numerically, making them appealing as a general tool. The rationale behind *k*-space methods and the *k*-space approach to the numerical modeling of photoacoustic waves in fluids are covered in this paper. Three existing *k*-space models are applied to photoacoustics and demonstrated with examples: an exact model for homogeneous media, a second-order model that can take into account heterogeneous media, and a first-order model that can incorporate absorbing boundary conditions.
 [DOI: 10.1121/1.2717409]

PACS number(s): 43.35.Ud, 43.20.Px [TDM] Pages: 3453–3464

I. INTRODUCTION

The photoacoustic (PA) effect, in which the absorption of light leads to the generation of an acoustic wave via the thermoelastic expansion of the absorbing region, has found application in many fields,[1] some of the most important being spectroscopy,[2,3] microscopy,[4–6] and biomedicine.[7] Biomedical photoacoustic tomography (PAT), in particular, has received increasing attention in recent years.[8,9] Both clinical and life sciences applications have been proposed, including imaging of the breast,[10] vasculature,[11] and small animals.[12,13] As soft tissue is usually highly optically scattering, imaging to high resolution using purely optical means is difficult. However, for acoustic waves, even up to tens of megahertz, the scattering is considerably lower. PAT can therefore combine the good resolution of ultrasound (<100 μm) with the high contrast and spectroscopic advantages offered by images related to optical absorption.

Most PAT reconstruction algorithms assume that both the sound speed and density in the sample are uniform.[7,14–22] which is not true of soft tissue in general, particularly at high frequencies. The extent to which the naturally occurring acoustic heterogeneities distort the PAT images remains largely an open question. One way to answer such questions without undertaking extensive experimental studies is to simulate the experimental measurements using a numerical forward model, so that the effect of heterogeneities on image resolution and artifact generation can be studied systematically. A further application of a photoacoustic forward model is in model-based image reconstruction algorithms for PAT.[23,24] Model-based image reconstructions make no assumptions of acoustic homogeneity, and form an image by iteratively updating a forward model. For iterative reconstruction algorithms such as this to be practical, it is imperative that the forward model is computationally efficient.

A numerical, time domain, model based on Poisson's solution to the wave equation has been widely used for calculating the pressure time history at a point from a photoacoustically generated source in homogeneous media.[25,26] This model has also been adapted to accommodate small sound speed heterogeneities.[23] More recently, finite difference[27] and (frequency domain) finite element methods[28] have been presented as techniques for modeling photoacoustics in heterogeneous media. This paper is concerned with wave number domain or *k*-space methods, which can achieve the same accuracy as the above-mentioned methods despite using a much coarser spatial grid, and can take much larger time steps without causing instabilities. *k*-space methods are therefore computationally efficient, and are ideal as forward models in model-based image reconstruction algorithms for PAT. In addition to being efficient and

[a]Electronic mail: bencox@mpb.ucl.ac.uk

accurate, numerical *k*-space models in both two and three dimensions are straightforward to encode. In view of these advantages, it is surprising that *k*-space methods are not more widely used for studying photoacoustic propagation. To date, photoacoustic propagation has been calculated using *k*-space methods only for homogeneous media.[29–31] Here we review two further *k*-space models,[32,33] originally derived to describe ultrasonic scattering due to heterogeneous media, and by adding a photoacoustic source term to each, demonstrate their use in photoacoustics with several examples.

II. FORWARD MODELS IN PHOTOACOUSTICS

A. Photoacoustic wave equation

The forward or direct problem in photoacoustics is to predict the acoustic field as a function of time following the absorption of an optical pulse. If a region of a fluid is heated by the absorption of a pulse of light, then a sound wave is generated. In a stationary fluid, under conditions whereby the sound generation mechanism is thermoelastic and terms containing the viscosity and thermal conductivity are negligible—a regime called thermal confinement—the acoustic pressure, $p(\mathbf{x},t)$, in the linear acoustic approximation and in the absence of absorption, obeys

$$\frac{\partial^2 p}{\partial t^2} - c^2 \rho \nabla \cdot \left(\frac{1}{\rho} \nabla p \right) = \Gamma \frac{\partial \mathcal{H}}{\partial t}, \tag{1}$$

where the sound speed $c(\mathbf{x})$ and density $\rho(\mathbf{x})$ vary with position $\mathbf{x}$. Γ is a dimensionless constant called the Grüneisen parameter, which indicates the efficiency of conversion of absorbed optical energy (heat) to pressure, and is defined as $\Gamma = c^2\beta / C_p$, where β is the volume thermal expansivity and C_p is the specific heat capacity. $\mathcal{H}(\mathbf{x},t)$ is the heat energy per unit volume and per unit time deposited in the fluid and, like the pressure p, will depend, in general, on both position $\mathbf{x}$ and time t. When the sound speed and density are uniform, so $c(\mathbf{x}) = c_0$ and $\rho(\mathbf{x}) = \rho_0$, then Eq. (1) becomes

$$(\partial^2/\partial t^2 - c_0^2 \nabla^2) p = \Gamma \, \partial \mathcal{H}/\partial t. \tag{2}$$

If the photoacoustic source term $\mathcal{H}(\mathbf{x},t)$ is stationary, then it may be separated into spatial and temporal components $\mathcal{H}(\mathbf{x},t) = H_x(\mathbf{x}) H_t(t)$, where $H_x(\mathbf{x})$ is the heat deposited in the fluid per unit volume, and $H_t(t)$ describes the temporal shape of the pulse, normalized so that the integral of H_t is unity. For instance, if the heating pulse is assumed Gaussian then

$$H_t(t) = \frac{e^{-(t/\tau)^2}}{\tau \sqrt{\pi}}. \tag{3}$$

As $\tau \to 0$ this pulse $H_t(t) \to \delta(t)$ so if $c\tau$ is much shorter than a typical distance across the heated region, a regime known as "stress confinement," then the PA source term may be considered to be instantaneous and well-represented by the time-derivative of a δ function. In this case, the forward problem reduces to the initial value problem (IVP) for the homogeneous wave equation

$$(\partial^2/\partial t^2 - c_0^2 \nabla^2) p = 0 \tag{4}$$

with initial conditions

$$p|_{t=0} = \Gamma H_x, \quad \partial p/\partial t|_{t=0} = 0. \tag{5}$$

In the examples below we assume $\mathbf{x} \in \mathbb{R}^2$, as it is more straightforward to display images of a two-dimensional (2D) wave field, but all the algorithms may be easily extended to three spatial dimensions.

B. Models based on Poisson's solution

Under conditions of thermal confinement, i.e., instantaneous heating, Poisson's solution to the IVP in Eqs. (4) and (5) may be used to calculate the acoustic field

$$p(\mathbf{x},t) = \frac{\Gamma}{4\pi c_0} \frac{\partial}{\partial t} \int_{A(t)} \frac{H_x(\mathbf{x}')}{R} dA, \tag{6}$$

where $R = |\mathbf{x} - \mathbf{x}'|$, and $A(t)$ is the surface on which $R = c_0 t$ and is thus a function of time. The optical excitation pulse is taken to occur at $t=0$. This equation has been implemented numerically by a number of authors[25,26] by defining $H_x(\mathbf{x})/R$ on a mesh and summing the contributions that lie within the two circles $A(t)$ and $A(t+\Delta t)$ for $t = 0, \Delta t, \ldots$. The resulting time series is numerically differentiated to give the acoustic pressure. This model was extended to take into account the spatial averaging effect of a finite-sized detector by Köstli and Beard,[34] by convolving the detector volume $D(\mathbf{x})$ with $H_x(\mathbf{x})$ prior to carrying out the integration over A. Xu and Wang[23] investigated the effects of sound speed heterogeneities on breast thermoacoustic tomography by developing analytical expressions for the effect on the amplitude and delay of a pulse. They concluded that the effect of a time delay is more important in imaging, and so adapted Poisson's model to incorporate a first-order correction for different times-of-flight through the heterogeneous medium, by warping the surface A.

The advantage of this model is that it is intuitive, and can be an aid to visualizing the forward problem. It is, however, computationally inefficient, and limited in the degree to which it can model boundaries or heterogeneous acoustic properties. For more complex situations, one approach is to turn to two well-established tools of numerical modeling: finite element and finite difference methods.

C. Finite element and finite difference methods

The finite element (FE) method is a popular and powerful method for calculating numerical solutions to partial differential equations because of its flexibility, accuracy, and rigorous mathematical foundations. In this method, the solution is represented by a linear combination of N-dimensional basis functions defined on the computational domain, and the unknown amplitudes of these functions are calculated to give a solution, exact at N nodes and approximate in between. The flexibility in the choice of basis functions allows domains and heterogeneities of any shape to be well-approximated, and, more important, the basis functions can be chosen to have support over only a small part of the domain, so calculation of the unknown amplitudes can be reduced to a sparse matrix equation for which there are efficient solvers available. Heterogeneous material properties can be straightforwardly included, and the well-developed

mathematical fundamentals of the technique allow thorough analyses of errors and sensitivities. Encoding the FE method, however, is not as straightforward as the finite difference (FD) or *k*-space methods discussed in the following, although many commercial packages are now available to ease this burden. Another disadvantage is that, when solving wave problems with the FE method, about 10 nodes per wavelength are required to represent the field accurately, so high-frequency, large-scale, applications soon become intractable. Jiang *et al.*[28] have used the FE method to find low frequency solutions of a PA Helmholtz-like equation which includes terms for sound speed heterogeneity and acoustic absorption.

Another group of techniques that is in widespread use for finding numerical solutions to partial differential equations is that of finite differences, in which derivatives in the partial differential equation are approximated by differences, thus converting the PDE into a difference equation which can be solved numerically. FD models are less flexible than FE models because, usually, a regular computational mesh must be used. The high-frequency sampling requirement, which is disadvantageous to FE methods, is a problem here too. Nevertheless, the popularity of FD methods endures, perhaps because of their conceptual simplicity. Huang *et al.*[27] describe a FD time-domain simulation of PA propagation, which includes nonlinear terms and dissipative effects, and is therefore more general than any of the other models described in this paper, although the underlying equations are correspondingly more complex. For biomedical applications, the assumptions of linearity and thermal confinement—which are required for all the models in this paper—seem to be valid, and allow considerable simplification of the governing equations, and therefore of the model.

For time domain problems, it is common practice to use a FD approximation to the time derivative, whether the spatial part of the solution is solved using FD or FE methods. Approximating the time derivative in this way can introduce numerical dispersion, in which the speed of the wave depends, erroneously, on its frequency, thus distorting the shape of pulses. To avoid this, small time steps must be taken, further reducing the efficiency of both FE and FD time domain models.

D. Pseudospectral and *k*-space models

The FE and FD methods, although excellent for many applications, become cumbersome and slow when modeling large scale, high-frequency acoustics applications, due to the requirements for many mesh points for wavelength, and small time steps required to minimize unwanted dispersion. In this section we briefly describe the pseudospectral (PS) method, which can help reduce the first of these problems, and *k*-space propagators, to overcome the second.

In a simple FD scheme, the gradient of the field is estimated by fitting a straight line between its values at two mesh points. A better estimate of the gradient could be obtained by fitting a higher-order polynomial to a greater number of points, and calculating the derivative of the polynomial. The more points used, the higher the degree of polynomial required, and the more accurate the estimate of the derivative. The PS method takes this idea further and fits a Fourier series to all the data on each line of the mesh. This choice of interpolating function assumes that the solution is periodic (the values and the derivatives at both ends of each line of the mesh are the same) which will rarely be the case. The "wrapping" effects of this assumption are common to PS and *k*-space methods and are seen in the example in Sec. IV A. Such effects can often be ameliorated using absorbing boundary conditions (see Sec. V and references therein). There are two significant advantages to using Fourier series. The first is that the amplitudes of the Fourier components can be calculated efficiently using the Fast Fourier transform (FFT), and the gradient calculated simply as $\mathcal{F}^{-1}\{ik_x\mathcal{F}\{p(x)\}\}$, where $\mathcal{F}\{\cdot\}$ is a Fourier transform and $\mathcal{F}^{-1}\{\cdot\}$ its inverse. The second advantage is that the basis functions assumed by the FT are sinusoidal, so only two nodes per wavelength are required in order to describe a wave, rather than 10+ in the FE and FD methods.

Now, both PS time-domain (PSTD) and *k*-space methods calculate the spatial gradients using FFTs, as just described. However, whereas the PSTD method approximates the temporal gradient with a finite difference, in *k*-space methods the field is propagated forward in time according to a *k*-space propagator, which is exact for homogeneous media, and, for heterogeneous media, allows much larger time steps for similar accuracy and stability to FD methods.[32,33,35–39] In Ref. 39 the *k*-space method is shown to give more accurate results than a second-order FD method for elastic wave propagation even when the time step is larger. References 32 and 33 describe benchmark studies of the accuracy of the *k*-space method in comparison with a leapfrog PSTD method and a time domain FD method. Examples of propagation through samples realistic of soft tissue were calculated using each model for a range of values of the Courant-Friedrichs-Lewy number, $\mathrm{CFL} \equiv c_0 \Delta t / \Delta x$, and it is shown that the error norm increases much more slowly with CFL for the *k*-space method than for either of the other two methods. It was also shown that the number of mesh points per wavelength required for a given accuracy is much less (≈ 3 as opposed to ≈ 10) for the *k*-space method than for the FD method.

As well as being efficient by virtue of the reduced point-per-wavelength requirement, the use of the FFT to calculate the gradients in *k* space, and larger time steps made possible by the *k*-space time propagator, another attraction of *k*-space models is that they are straightforward to encode. In this paper, three efficient, *k*-space forward models of photoacoustic wave generation and propagation are described. All three calculate the acoustic field as a function of time, given an arbitrary distribution of absorbed optical energy. This first model applies only to homogeneous media,[29] whereas the second[32] and third[33] include the effects of acoustic heterogeneities, i.e., spatial variations in the sound speed and density. The differences between the second and third are that the latter can incorporate absorbing boundary conditions and bulk acoustic absorption.

III. *k*-SPACE MODEL FOR A HOMOGENEOUS MEDIUM

When the sound speed and density are constant everywhere, then the photoacoustic waves propagate according to Eq. (2). Following spatial Fourier transformation, Eq. (2) becomes an ODE in time, describing the motion of plane waves with wave vector $\mathbf{k}=(k_x,k_y)$,

$$\left(\frac{d^2}{dt^2}+(c_0k)^2\right)\hat{p}=\hat{S}(t), \tag{7}$$

where the caret indicates a function in $\mathbf{k}$ space, and k is the modulus of $\mathbf{k}$. The source term $\hat{S}(t)$ is given by

$$\hat{S}(t)=\Gamma\hat{H}_x\frac{\partial H_t}{\partial t}. \tag{8}$$

The Green's function solution to Eq. (7) is

$$\hat{p}(\mathbf{k},t)=\int_0^t \hat{g}(t-t')S(t')dt' \tag{9}$$

$$=\Gamma\hat{H}_x\int \hat{g}(t-t')\frac{dH_t}{dt'}(t')dt', \tag{10}$$

where the Green's function $\hat{g}$ is a solution to $d^2\hat{g}/dt^2+(c_0k)^2\hat{g}=\delta(t)$ and is given by

$$\hat{g}(\mathbf{k},t)=\begin{cases}0, & t<0\\ \sin(c_0kt)/(c_0k), & t\geqslant 0.\end{cases} \tag{11}$$

When $H_t(t)=\delta(t)$, an instantaneous pulse at $t=0$, the solution for the pressure becomes

$$\hat{p}(\mathbf{k},t)=\Gamma\hat{H}_x\int\left(\frac{\sin(c_0k(t-t'))}{c_0k}\right)\delta'(t')dt'$$

$$=\Gamma\hat{H}_x\cos(c_0kt) \tag{12}$$

so the acoustic field at time t following an optical pulse at $t=0$ can be calculated using

$$p(\mathbf{x},t)=\Gamma\mathcal{F}^{-1}\{\hat{H}_x(\mathbf{k})\cos(c_0kt)\}. \tag{13}$$

This is an exact solution, so the acoustic field can be calculated directly for any time t without having to step through the previous times from $t=0$. In this sense, the $\cos(ckt)$ term in Eq. (13) can be considered as an exact time propagator. (To calculate pressure time histories on just a single plane perpendicular to the axis of symmetry in a radially symmetric field, the vertical wave-number-frequency mapping technique described in Cox and Beard[29] is considerably more efficient.)

It is instructive to see that the solution in Eq. (13) can be written as an explicitly time-stepping, finite-difference-style solution, in which the field at $t+\Delta t$ is calculated from the field at times t and $t-\Delta t$. Consider the transformed field, $\hat{p}(\mathbf{k})$, at the two times $t+\Delta t$ and $t-\Delta t$:

$$\hat{p}(t+\Delta t)=\Gamma\hat{H}_x\cos(c_0k(t+\Delta t))$$

$$=\Gamma\hat{H}_x(\cos(c_0kt)\cos(c_0k\Delta t)$$

$$-\sin(c_0kt)\sin(c_0k\Delta t)), \tag{14}$$

$$\hat{p}(t-\Delta t)=\Gamma\hat{H}_x\cos(c_0k(t-\Delta t))$$

$$=\Gamma\hat{H}_x(\cos(c_0kt)\cos(c_0k\Delta t)$$

$$+\sin(c_0kt)\sin(c_0k\Delta t)). \tag{15}$$

So,

$$\hat{p}(t+\Delta t)+\hat{p}(t-\Delta t)=2\Gamma\hat{H}_x\cos(c_0kt)\cos(c_0k\Delta t)$$

$$=2\hat{p}(t)\cos(c_0k\Delta t)$$

$$=2\hat{p}(t)(1-2\sin^2(c_0k\Delta t/2)) \tag{16}$$

and rearranging gives

$$\hat{p}(t+\Delta t)-2\hat{p}(t)+\hat{p}(t-\Delta t)=-4\sin^2(c_0k\Delta t/2)\hat{p}(t). \tag{17}$$

This is a time-stepping solution for which steps Δt of any size may be used without introducing error. This is an exact rearrangement of Eq. (13), so by using the initial conditions $\hat{p}(-\Delta t)=\Gamma\hat{H}_x\cos(c_0k\Delta t)$ and $\hat{p}(0)=\Gamma\hat{H}_x$, exactly the same solutions for any $t>0$ will be calculated. By comparing Eq. (17) to a pseudospectral, leapfrog FD scheme, based on Eq. (7) in the absence of the source term,

$$\frac{\hat{p}(t+\Delta t)-2\hat{p}(t)+\hat{p}(t-\Delta t)}{\Delta t^2}=-(c_0k)^2\hat{p}(t) \tag{18}$$

we can see that the $4\sin^2(c_0k\Delta t/2)$ term in Eq. (17) has replaced the term $(c_0k\Delta t)^2$ in Eq. (18). For small time steps these are equal, but for larger time steps the latter leads to numerical dispersion whereas the former provides an exact, dispersion-free, solution. Of course, with δ-function heating, there is no need for such a time stepping scheme as we have an exact propagator for arbitrarily large time steps, Eq. (13). Indeed, the solution for a finite-duration Gaussian excitation pulse could be obtained by multiplying the Fourier transform of Eq. (3) to the other k-space terms in Eq. (13). However, when considering a source with an arbitrary temporal pulse shape, or propagation through heterogeneous media, a time-stepping scheme may be required. We can extend the time-stepping scheme in Eq. (17) to include a source with an arbitrary pulse shape:

$$\hat{p}(t+\Delta t)-2\hat{p}(t)+\hat{p}(t-\Delta t)=-4\sin^2(c_0k\Delta t/2)\left(\hat{p}(t)-\frac{\hat{S}(t)}{(c_0k)^2}\right). \tag{19}$$

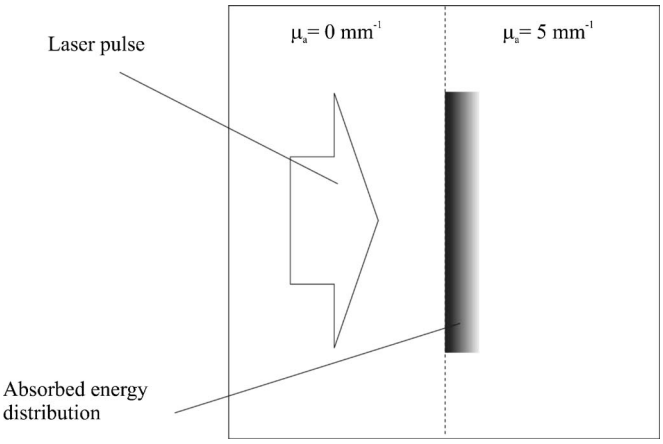

FIG. 1. A collimated laser beam with a 6-mm-diam tophat profile, indicated with an arrow, is incident on an optically absorbing half-space, the surface of which is marked by a dotted line. The optical absorption coefficient $\mu_a = 5$ mm^{-1}. The absorbed energy distribution decays exponentially from the boundary according to the Beer-Lambert law. The laser fluence at the surface was 10 mJ/cm^2 (i.e., 10 mJ/cm per cm into the plane of the paper). The sound speed and density were 1500 m/s and 1000 kg/m^3, respectively, and the Grüneisen parameter $\Gamma = 0.11$. The evolution of this acoustic field is shown in Fig. 2.

A. Example: Laser beam incident on an absorbing half-space

A two-dimensional (2D) example of a tophat laser beam incident on a pure (nonscattering) absorber is used to demonstrate the homogeneous model in Eq. (19). Figure 1 shows the arrangement: A collimated laser beam with a 6 mm diameter tophat profile, indicated by an arrow, is incident on an optically absorbing half-space, the surface of which is marked by a dotted line. The optical absorption coefficient $\mu_a = 5$ mm^{-1}. The absorbed optical energy results in a spatially varying heating function, $\mathcal{H}_x(\mathbf{x})$, which decays exponentially from the boundary according to the Beer-Lambert law, and is shown in Figs. 1 and 2 (top left) as a dark region. As this example has 2D symmetry, with no variation into or out of the plane of the paper, the tophat beam effectively models a three-dimensional (3D) line source. The laser fluence at the surface of the absorber was set to 10 mJ/cm^2 (i.e., 10 mJ/cm per cm into the plane of the paper). The sound speed and density were 1500 m/s and 1000 kg/m^3, respectively, and the Grüneisen parameter $\Gamma = 0.11$, their values in water (the major constituent of soft tissue). The 2D computational grid of 10 mm $\times$ 10 mm, was divided into 600×600 squares, which limited the maximum frequency to about 60 MHz. The absorbed energy distribution was smoothed to ensure there were no wave number components higher than about $0.8\pi/\Delta x$ where Δx is the grid spacing. The time $t = 0$ was defined as the midway point of the temporal heating pulse, Eq. (3), whose pulse width was $\tau = 8.33$ ns, and so the program was set to begin at a time well before this so as to include all of the first half of the pulse. The validity of the use of a Gaussian function to approximate the instantaneous, δ-function, heat deposition is examined in the following. All the models in this paper were written in MATLAB (Release 13, The Mathworks, Inc.).

Figure 2 shows the pressure field as it evolves, at times 0, 0.33, 0.66, and 1 μs following the laser pulse. This acoustic pressure field can be described as a combination of two compressive plane waves and two circular, edge waves which have a tensile component. The pressure as a function of time for a point located at the point $(-1, 0)$ is shown in Fig. 6.

B. Example: Line source with a Gaussian profile

The use of a Gaussian temporal function to approximate a δ function (instantaneous heating) is valid for a pulse whose duration is much shorter than the acoustic travel time across the region of support of the source $\mathcal{H}_x$. (The "stress confinement" condition.) With the above example, this becomes the requirement that the pulse width $\tau \ll 1/(\mu_0 c_0) = 133$ ns, so the condition was met. An implication is that the less stringent assumption of "thermal confinement," required for Eq. (1) to hold, is also valid. To check this assumption, a comparison has been made with an analytical solution.

Diebold and Sun[40] provide an analytical solution for an infinitely long, cylindrical source distribution with a Gaussian radial profile that is instantaneously deposited at $t = 0$. This can be modeled in 2D by assuming the axis of the cylinder is directed perpendicular to the 2D plane. A comparison between Diebold's solution and the homogeneous k-space model shows that it is reasonable to model the temporal dependence of the photoacoustic source term with a Gaussian when the stress confinement condition applies. For a source profile with a radial width $\sigma = 1$ mm, the stress confinement condition is $\tau \ll \sigma/c_0 = 0.67$ μs. To calculate Fig. 3 τ was set to 0.01 μs, well within this criterion. Figure 3 shows how the acoustic pressure varies with time at a point

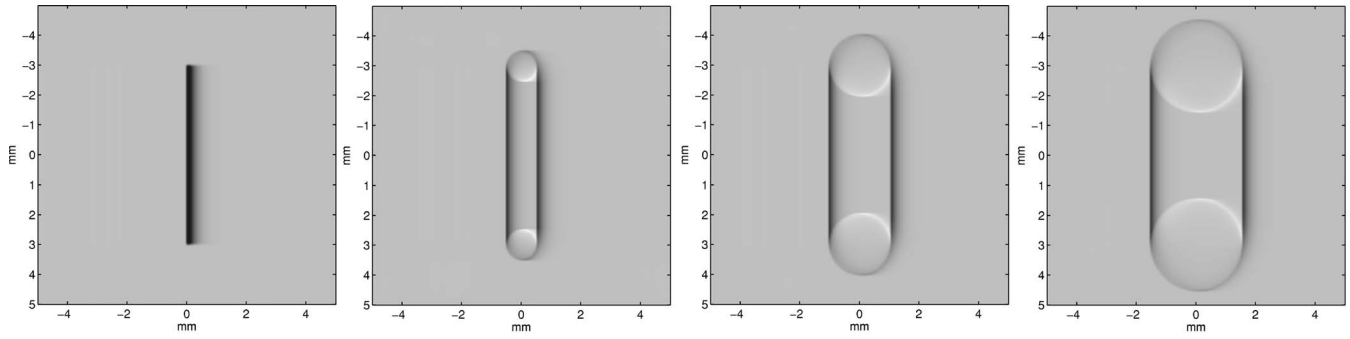

FIG. 2. The evolution of the photoacoustic pressure field for the arrangement shown in Fig. 1. The acoustic pressure is shown at times $t = 0$, 0.33, 0.66, and 1 μs following the laser pulse, calculated using the homogeneous model of Sec. III. The linear grey scale is from -10 kPa (white) to 40 kPa (black).

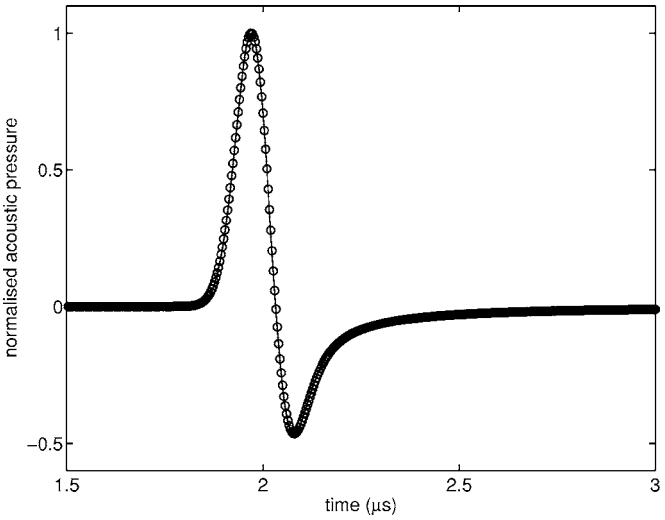

FIG. 3. Acoustic pressure 3 mm off axis for an infinitely long impulsive heating source with a Gaussian radial profile. Analytic solution (solid line) which assumes instantaneous (δ function) heat deposition, and k-space model for a homogeneous medium (circles), which uses a Gaussian approximation to the temporal δ function. When the stress confinement condition holds, as in this case, this approximation gives good agreement. The Gaussian radial width $\sigma=1$ mm.

3 mm off axis. The time series were calculated using Diebold's solution (solid line) and the homogeneous k-space model (circles), and they show good agreement. Additional examples, comparing a model of photoacoustic propagation based on Poisson's solution, Eq. (6), to the k-space model of Eq. (13) can be found in Cox and Beard.[29]

IV. HETEROGENEOUS MEDIUM: SECOND-ORDER *k*-SPACE MODEL

An accurate model of the propagation of PA waves in tissue must include the effects of the sound speed and density heterogeneities. We follow the approach taken by Mast *et al.*[32] By defining a new variable $f(\mathbf{x},t)\equiv p(\mathbf{x},t)\rho(\mathbf{x})^{-1/2}$, sometimes called a Liouville transform, the wave equation for inhomogeneous media, Eq. (1), may be rearranged into the homogeneous form of the wave equation with effective source terms due to sound speed and density heterogeneities on the right-hand side:

$$\nabla^2 f - \frac{1}{c_0^2}\frac{\partial^2 f}{\partial t^2} = \frac{1}{c_0^2}\left(q + \frac{\partial h}{\partial t} + \frac{\partial^2 v}{\partial t^2}\right), \tag{20}$$

where c_0 is a fixed sound speed, usually chosen as the maximum of $c(\mathbf{x})$ for reasons of stability. There are three terms on the right-hand side corresponding to waves generated in three different ways: at changes in density, Eq. (21), photoacoustically, Eq. (22), and at changes in sound speed, Eq. (23):

$$q(\mathbf{x},t) = c_0^2\sqrt{\rho(\mathbf{x})}\nabla^2(\rho(\mathbf{x})^{-1/2})f(\mathbf{x},t), \tag{21}$$

$$h(\mathbf{x},t) = -\rho(\mathbf{x})^{-1/2}\Gamma\mathcal{H}(\mathbf{x},t), \tag{22}$$

$$v(\mathbf{x},t) = (c_0^2/c(\mathbf{x})^2 - 1)f(\mathbf{x},t). \tag{23}$$

As the heating pulse is assumed to be Gaussian, Eq. (3), the photoacoustic source term becomes

$$\frac{\partial h(\mathbf{x},t)}{\partial t} = \rho^{-1/2}\Gamma H_x(\mathbf{x})\left(\frac{2te^{-(t/\tau)^2}}{\tau^3\sqrt{\pi}}\right). \tag{24}$$

Now, by introducing the auxiliary field, $w=f+v$, and transforming from $\mathbf{x}$ space to $\mathbf{k}$ space, Eq. (20) may be rearranged into the form

$$\frac{\partial \hat{w}^2}{\partial t^2} = (c_0 k)^2(\hat{v} - \hat{w}) - \hat{q} - \frac{\partial \hat{h}}{\partial t}, \tag{25}$$

where ∇^2 has been replaced by $-k^2$. Eliminating f from Eqs. (21) and (23) gives

$$\hat{q}(\mathbf{k},t) = c_0^2\mathcal{F}\{\tilde{\rho}(\mathbf{x})(w(\mathbf{x},t) - v(\mathbf{x},t))\}, \tag{26}$$

$$\hat{v}(\mathbf{k},t) = \mathcal{F}\{(1 - (c(\mathbf{x})/c_0)^2)w(\mathbf{x},t)\}, \tag{27}$$

where we have used the shorthand $\hat{\rho}\equiv\rho^{1/2}\nabla^2(\rho^{-1/2})$. By comparing Eq. (25) with Eqs. (7) and (19) we see that it may be approximated by

$$\hat{w}(\mathbf{k},t+\Delta t) - 2\hat{w}(\mathbf{k},t) + \hat{w}(\mathbf{k},t-\Delta t) \approx 4\sin^2\left(\frac{c_0 k\Delta t}{2}\right)\left[\hat{v} - \hat{w}\frac{(\hat{q} + \partial\hat{h}/\partial t)}{(c_0 k)^2}\right]. \tag{28}$$

Given two initial conditions, $\hat{w}(\mathbf{k},-\Delta t)$ and $\hat{w}(\mathbf{k},0)$, this difference equation may be used to step the field $\hat{w}$ forward in time. Here, both initial conditions are set to zero. In the homogeneous limit, this gives exact solutions, and is equivalent to Eq. (19).

So, with $w(-\Delta t)=w(0)=0$ and $\partial h/\partial t$ known for all t from Eq. (24), the procedure for calculating the pressure field as function of time using this model is as follows: For every t calculate, in this order, $\hat{v}(\mathbf{k},t)$ using Eq. (27), $v(\mathbf{x},t)$ by transforming $\hat{v}$, $\hat{q}(\mathbf{k},t)$ using Eq. (26), and $\hat{w}(\mathbf{k},t+\Delta t)$ using Eq. (28). The acoustic pressure may then be obtained from $p(\mathbf{x},t)=\rho^{1/2}(w(\mathbf{x},t)-v(\mathbf{x},t))$.

Examples including acoustic heterogeneities. The example of a light pulse with a tophat profile, used in Sec. III A to demonstrate the homogeneous model of Eq. (19), is adapted to show the effect of an acoustic homogeneity on the field, using the above-described model. A single, circular heterogeneity with sound speed and density half of their values in the surrounding tissue was included as shown in Fig. 4. All other parameters in the example were left unchanged. While such a great change in sound speed is rare within soft tissue, even greater contrasts can be found at air or vapor pockets. The main reason for choosing a large contrast here was in order to produce a significant reflection and distortion of the wavefront to best show the capabilities of the model. The density and sound speed distributions were smoothed to remove wavenumber components higher than about $0.8\pi/\Delta x$. The time increment Δt was set to 2.78 ns, well inside the Nyquist requirement (Sec. VI). This model took about 2 s per time step on a 2 GHz PC with 768 Mbytes RAM.

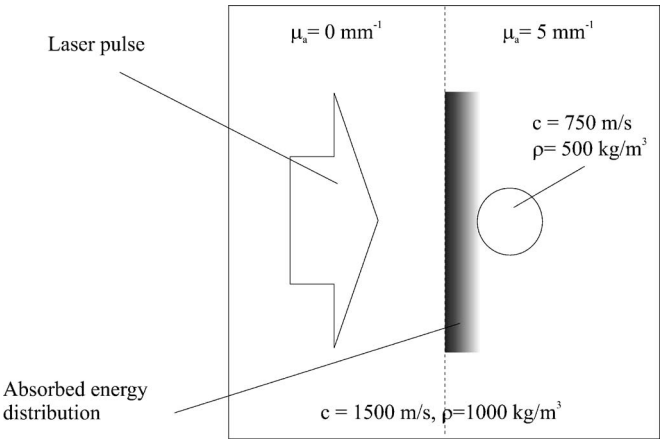

FIG. 4. An example identical to Fig. 1, except for the circular heterogeneity with sound speed and density half that of the surrounding medium.

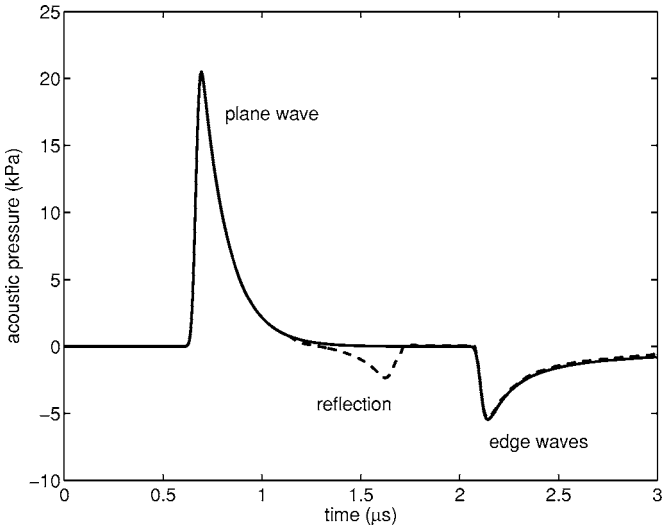

FIG. 6. Pressure time histories calculated for the point (−1,0) (see Figs. 2 and 5), for both the acoustically homogeneous (solid line) and heterogeneous (dashed line) cases. The additional wave, reflected from the acoustic inhomogeneity, is clear.

Figure 5, like Fig. 2, shows the evolution of the acoustic wave with time. The acoustic pressure is shown at times $t=0$, 0.33, 0.66 and 1 μs following the laser pulse. The slower passage of the wavefront through the circular region of lower sound speed, and the resulting distortion of the plane wavefront is clearly visible. The wave reflected from the heterogeneity can also be seen. Figure 6 shows time series calculated for a point 1 mm to the left of the center of the image, for both the acoustically homogeneous (solid line) and heterogeneous (dashed line) cases. The reflected wave can be seen arriving at about 1.5 μs, in between the plane and edge wave components of the initial wavefield.

The tophat example, Figs. 5 and 6, was chosen to show clearly the wavefront distortion and reflection caused by a single acoustic heterogeneity. The following example shows the acoustic radiation from three circular sources, which could, for instance, be used to represent blood vessels. Figure 7 shows the pressure field at times of 0, 0.33, 0.66,… 2.33 μs. The sound speed and density are 1500 m/s and 1000 kg/m^3, respectively, and the position of a rectangular heterogeneity ($c=1000$ m/s, $\rho=750$ kg/m^3), which distorts the circular wavefront from the right-most tube, is indicated by a dotted line. It is a result of the periodicity inherent in the FFT, that when a wavefront reaches the boundary of the image, it "wraps around" and appears on the other side. This can be seen with the wave from the leftmost source, which appears on the right-hand side of the last three frames. For calculations of transient fields, it may be possible to use a sufficiently large computational domain to avoid this wrap-around problem, or if only the pressure at a single point is required, to stop the calculations before the first arrival of a wrapped wave reaches that point. Nevertheless, for simulating measurements over an array it is not ideal to have to use a mesh considerably larger than the array in order to avoid the wrapped wave. For 3D problems, the number of elements in the mesh increases by eight times each time the linear dimensions are doubled, so the size of the computation soon becomes very large. Section V describes a first-order model for which absorbing boundary conditions can be prescribed, thus removing this problem.

V. HETEROGENEOUS MEDIUM: FIRST-ORDER *k*-SPACE MODEL

Both Eqs. (17) and (18) are discretizations of $\partial^2\hat{p}/\partial t^2 = -(c_0 k)\hat{p}$. Both models use $-k^2\hat{p}$ in place of the Laplacian, ∇^2, but whereas Eq. (17) uses a k-space time propagator, Eq. (18) employs a finite-difference approximation to time derivative. By rewriting Eq. (17) as

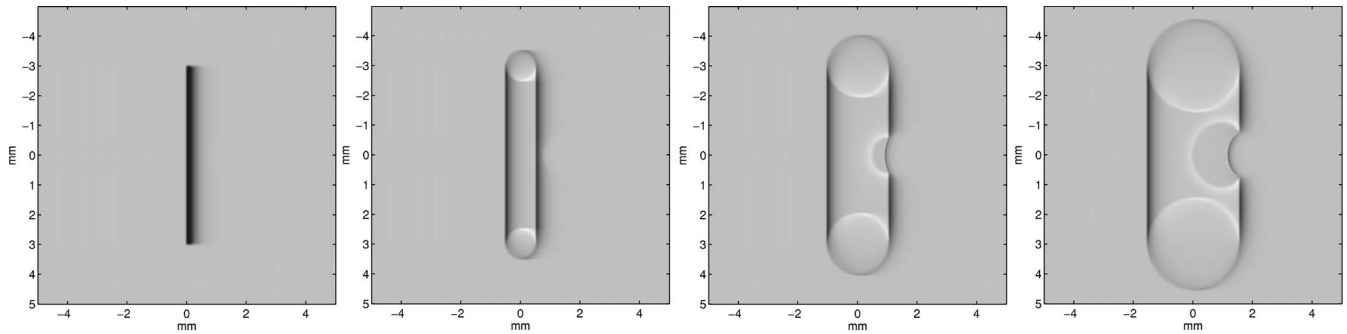

FIG. 5. The evolution of the photoacoustic pressure field for the arrangement shown in Fig. 4, including a circular heterogeneity. The acoustic pressure is shown at times $t=0$, 0.33, 0.66, and 1 μs following the laser pulse, calculated using the homogeneous model of Sec. III. The linear grey scale is from −10 kPa (white) to 40 kPa (black). The wave reflected from the heterogeneity, and the distorted wave front due to the reduced sound speed are clearly visible.

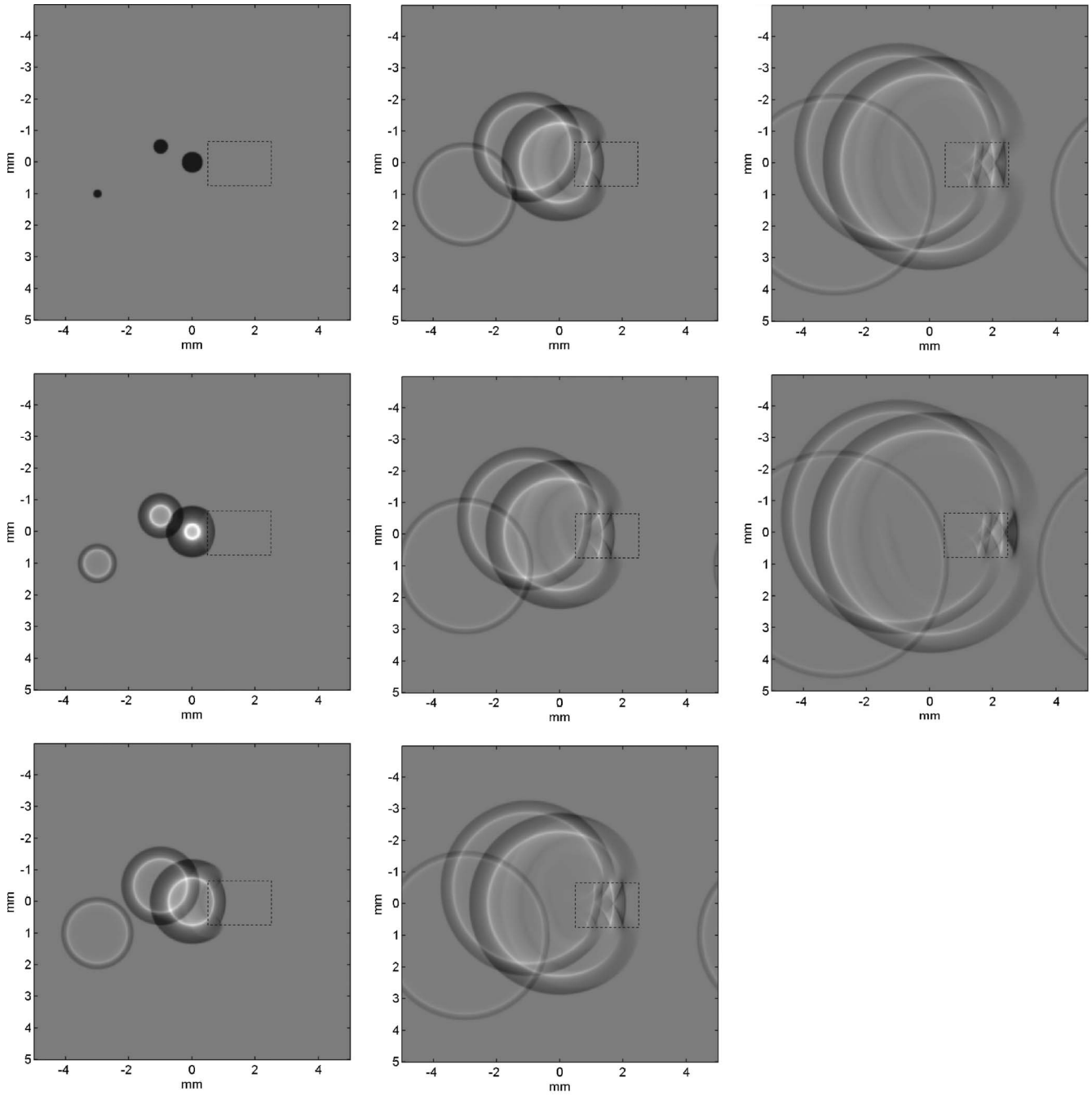

FIG. 7. The acoustic pressure field radiated from three circular photoacoustic sources is shown every 1/3 μs following an excitation light pulse. The sound speed and density are 1500 m/s and 1000 kg/m^3, respectively. The position of a rectangular acoustic heterogeneity (1000 m/s, 750 kg/m^3), which distorts the wavefront on the right of the image, is indicated by a dotted line. The periodic boundary conditions implicit in this model cause the acoustic waves to wrap around when it reaches the edge of the computational domain.

$$\frac{\hat{p}(t+\Delta t)-2\hat{p}(t)+\hat{p}(t-\Delta t)}{\Delta t^2\,\mathrm{sinc}^2(c_0k\Delta t/2)}=-(c_0k)^2\hat{p}(t) \tag{29}$$

it is clear that—so far as the time derivative is concerned—the *k*-space models described above can be thought of as FD models in which Δt^2 has been replaced by $\Delta t^2\,\mathrm{sinc}^2(c_0k\Delta t/2)$ in the approximation of $\partial^2/\partial t^2$. We can also see that replacing the spatial derivative $-k^2$ with $-k^2\,\mathrm{sinc}^2(c_0k\Delta t/2)$ would give the same solution. Exact solutions for the homogeneous case can be therefore be obtained by replacing the Laplacian with $-k^2\,\mathrm{sinc}^2(c_0k\Delta t/2)$ and calculating the temporal derivative using standard finite-differences. This observation is the motivation for the model described below.

While the two models described in Secs. III and IV are based on second-order equations, this *k*-space model, first described by Tabei *et al.*,[33] is based instead on the linearized conservation of momentum and mass equations. These first-order equations, with additional terms which act as an absorbing boundary condition (ABC) to overcome the wrap-around problem, are

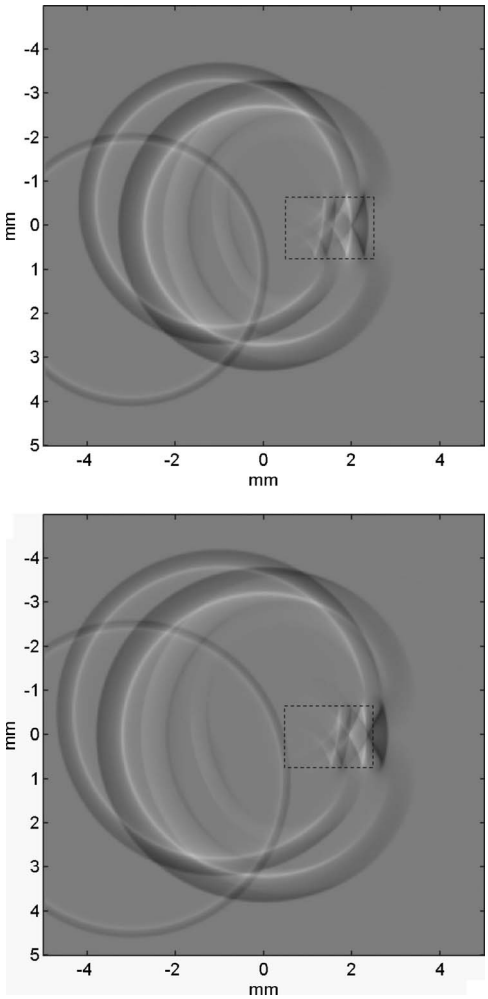

FIG. 8. The acoustic pressure field radiated from three circular photoacoustic sources, as shown in Fig. 7, at 2 and 2.33 μs following an excitation light pulse. The sound speed and density are 1500 m/s and 1000 kg/m^3, respectively. The position of a rectangular acoustic heterogeneity (1000 m/s, 750 kg/m^3), which distorts the wave front on the right of the image, is indicated by a dotted line. In contrast to the final two frames of Fig. 7, the acoustic waves do not wrap around when they reach the edge of the computational domain, but are rather attenuated to almost zero, due to the absorbing boundary condition.

$$\frac{\partial \mathbf{u}}{\partial t} = -\frac{\nabla p}{\rho} - \boldsymbol{\alpha} \cdot \mathbf{u}, \tag{30}$$

$$\frac{\partial p}{\partial t} = -\rho c^2 \nabla \cdot \mathbf{u} + \Gamma \mathcal{H} - (\alpha_x + \alpha_y) p, \tag{31}$$

where $\Gamma\mathcal{H}$ is the PA source term and the two terms containing $\boldsymbol{\alpha}=(\alpha_x(\mathbf{x}),\alpha_y(\mathbf{x}))$ represent the ABC. The principle advantage of using two first-order equations is that the vector $\mathbf{u}=(u_x,u_y)$ appears explicitly and it is therefore possible to introduce direction-dependent absorption, which cannot be done when only the scalar p is available. By defining the absorption $\boldsymbol{\alpha}$ to be zero everywhere except in a layer close to the edges of the domain, and in that layer to be zero in all directions except normal to the boundary, the amplitude of the waves leaving the domain (and only those leaving the domain) can be reduced to virtually nothing, and the wrap-around problem is eliminated. For instance, for a rectangular

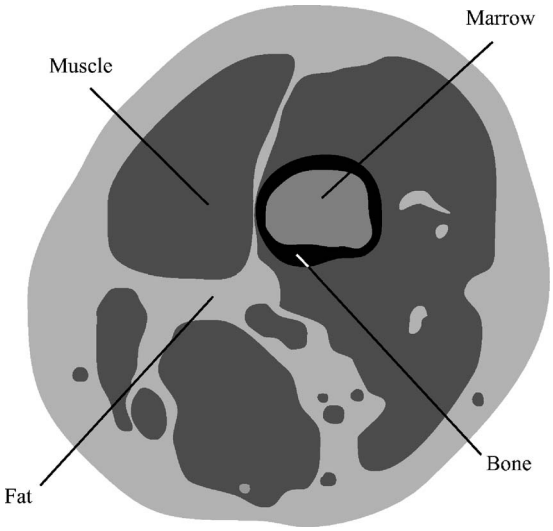

FIG. 9. The tissue properties for the example shown in Fig. 10. The sound speed and density of each region were set to: muscle, 1590 m/s and 1040 kg/m^3, fat, 1450 m/s and 900 kg/m^3, marrow, 1480 m/s and 1000 kg/m^3, and bone, 3200 m/s and 1900 kg/m^3.

domain, α_x would be chosen to be zero everywhere except within a layer close to the two boundaries perpendicular to the x axis, within which it increases nonlinearly to ensure all the outgoing energy is absorbed. α_y would be treated similarly in the y direction. This type of ABC is also called a perfectly matched layer.[41–43] Note that, as expected, Eqs. (30) and (31) can be reduced to the second-order wave equation, Eq. (1), when $\boldsymbol{\alpha}=0$.

As described earlier, instead of the usual k-space substitution for the Laplacian $\nabla^2 \rightarrow -k^2$, we use

$$\nabla^2 \rightarrow -k^2 \operatorname{sinc}^2(c_0 k \Delta t/2). \tag{32}$$

To solve Eqs. (30) and (31) numerically, however, expressions for $\partial/\partial x$ and $\partial/\partial y$ are required, not ∇^2. As $\nabla^2 \equiv \partial^2/\partial x^2 + \partial^2/\partial y^2$ and $k^2 = k_x^2 + k_y^2$, we choose $\partial/\partial x = ik_x \operatorname{sinc}(c_0 k \Delta t/2)$. In other words,

$$\frac{\partial p}{\partial x} = \mathcal{F}\{ik_x \operatorname{sinc}(c_0 k \Delta t/2)\hat{p}\} \tag{33}$$

and similarly for the gradient in the y direction. To enable the numerical calculations, the pressure is divided into two parts, $p=p_x+p_y$, and Eqs. (30) and (31) are split into four equations:

$$\dot{u}_x = -\nabla p/\rho - \alpha_x u_x, \tag{34}$$

$$\dot{u}_y = -\nabla p/\rho - \alpha_y u_y, \tag{35}$$

$$\dot{p}_x = -\rho c^2 \, \partial u_x/\partial x + \Gamma\mathcal{H}/2 - \alpha_x p_x, \tag{36}$$

$$\dot{p}_y = -\rho c^2 \, \partial u_y/\partial y + \Gamma\mathcal{H}/2 - \alpha_y p_y. \tag{37}$$

These equations are then discretized using a standard finite-difference scheme in time and Eq. (33) for the spatial derivatives. When solving for two variables, here the pressure p and particle velocity $\mathbf{u}$, it can be advantageous to use two offset (staggered) grids. This model with staggered grids (and also including bulk absorption due to relaxation pro-

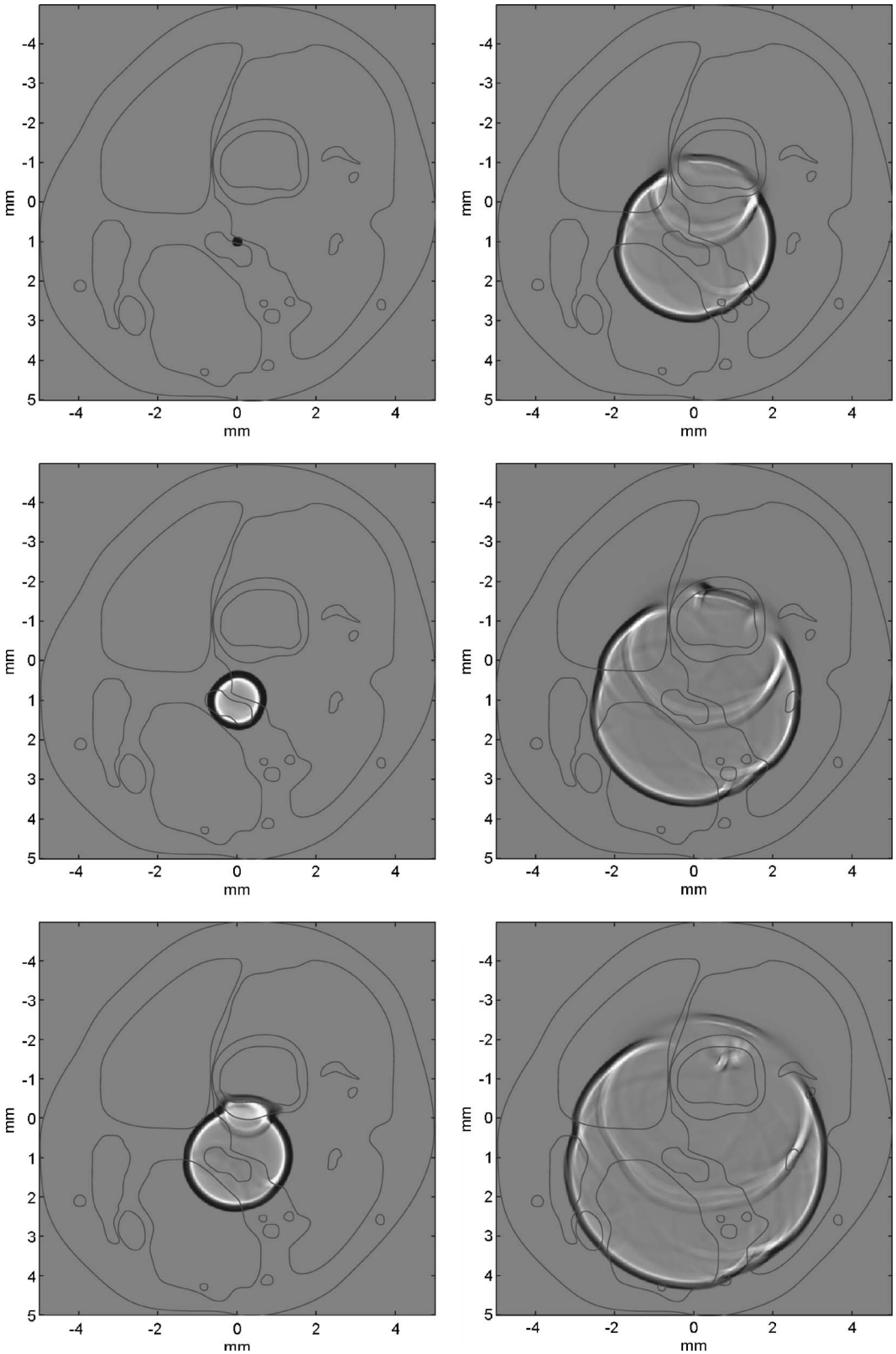

FIG. 10. Propagation of acoustic waves from a small, circular, photoacoustic source, through a heterogeneous medium with tissue-like properties (see Fig. 9). The frames are snapshots of the acoustic field at intervals of 0.21 μs following the optical pulse. The boundaries between the regions with different acoustic properties are superimposed, to show how the wave fronts are distorted by the heterogeneities.

cesses) is described in Tabei *et al.*[33] Such an implementation was used for the following examples.

Examples using the first-order model. The example shown in Fig. 7, which was calculated using the second-order model of Sec. IV, was recalculated using the first-order model described above which incorporated an absorbing boundary condition. In the last few frames in Fig. 7 the problem of the wave front wrapping around and appearing on the

far side of the image is evident. Figure 8 shows the pressure field at times corresponding to the last two frames of Fig. 7, but calculated by the first-order model. It is clear that the wrapping problem has been removed.

The final example, shown in Fig. 9, contains a degree of heterogeneity more representative of tissue. The model can account for continuously varying acoustic properties, although here the domain is divided into four types of tissue with different acoustic properties. The sound speeds and densities of the four tissue types were set to: muscle, 1590 m/s and 1040 kg/m^3, fat, 1450 m/s and 900 kg/m^3, marrow, 1480 m/s and 1000 kg/m^3, and bone, 3200 m/s and 1900 kg/m^3. A small circular PA source, that could for instance represent a blood vessel or a tumor, or a region with high chromophore concentration for another reason, is shown in the first frame of Fig. 10. This simple PA source was chosen so that the effect of the inhomogeneities on the wave fronts would be readily observable. It would be quite as straightforward to define a PA source with a complex geometry. The boundaries between the different tissue types have been superimposed on the images. The greyscale has been set the same in each image, which has led to some thresholding of the wave amplitude in the first few images. This allows the reflected and refracted waves to be seen more clearly. The frames are spaced by 0.21 μs. The most significant change to the circular wave front is, as expected, from the tissue-bone interface, where there is the greatest acoustic impedance change. The reflected wave and the reduced amplitude of the transmitted wave are visible. The distorting effect of the differences in the sound speed between the muscle and fat regions of the tissue can also be seen, for example, on the left-hand side of the wave.

VI. DISCUSSION

PA sources or distributions of acoustic properties that contain discontinuities or very large gradients at some points require high wave numbers in order to describe them accurately. In FFT-based, *k*-space methods, there is a limit to the highest permissible wave number, a requirement imposed by the need to prevent aliasing (when a wave number component is undersampled and appears at a lower wave number). There must be no components higher than the Nyquist wave number, defined as $0.5(2\pi/\Delta x)$, where Δx is the grid spacing. It is therefore important, when using *k*-space methods, to spatially smooth the acoustic properties and the spatial part of the source term in order to ensure there are no components at wave numbers above this limit. This could be considered to be a disadvantage to the *k*-space approach, because smoothed—and therefore approximate—versions of the sound speed, density, and source distributions are used when calculating the acoustic field. However, the high wave number components, which are removed by smoothing, would only have contributed to the high frequency part of the field, and as, in practice, all measurements are bandlimited by the detectors or ultrasonic absorption to some extent, only those wave numbers that contribute to the *measured* field are required for the model to simulate the acoustic pressure measurements accurately. In other words, when modeling measurements made by a pressure detector with a finite bandwidth, it is not necessary to include components of the field outside this bandwidth. Indeed, to obtain accurate simulations of data measured with a real, nonidealized, detector, a wave number model of the angle- and frequency-dependent response of a sensor[44] can be incorporated into a *k*-space model simply by multiplication, and without requiring an explicit convolution.

When calculating acoustic pressure time histories, it is important to ensure the time step, Δt, is sufficiently small to ensure the sampling rate is greater than the temporal Nyquist rate (i.e., half the maximum frequency). With *k*-space models this requirement is that Δt is less than the minimum value of $\Delta x/c$. For the above examples, Δt was $0.2-0.4\Delta x/c$.

All the models described in this paper are for photoacoustically generated waves propagating in fluids. In some circumstances it will be necessary to include the effect of shear waves on the propagation. *k*-space models for elastic wave propagation in solids have also been described,[39] and could be applied in these cases.

VII. SUMMARY

k-space models have been proposed as a straightforward and computationally efficient approach to modeling the forward problem in biomedical photoacoustics, in particular, to simulating, accurately, time series measured with a bandlimited detector. *k*-space models of photoacoustic waves can be significantly more efficient than corresponding FE and FD methods, as *k*-space methods address the particular difficulty of modeling high-frequency acoustic waves on a large scale by requiring fewer mesh points per wavelength and allowing larger time steps without reducing accuracy or introducing instability. The *k*-space method of numerical modeling of photoacoustic waves in fluids is described, and the rationale behind three particular *k*-space models (one for homogeneous media, one for heterogeneous media, and a model that can incorporate absorbing boundary conditions) has been explained. Examples of photoacoustic wave propagation in heterogenous, tissue-like, media are given.

ACKNOWLEDGMENT

This work has been supported by the Engineering and Physical Sciences Research Council, UK.

[1] A. C. Tam, "Applications of photoacoustic sensing techniques," Rev. Mod. Phys. **58**, 381–431 (1986).
[2] G. A. West, J. J. Barrett, D. R. Siebert, and K. V. Reddy, "Photoacoustic spectroscopy," Rev. Sci. Instrum. **54**, 797–817 (1983).
[3] J. G. Laufer, C. Elwell, D. Delpy, and P. Beard, "In vitro measurements of absolute blood oxygen saturation using pulsed near-infrared photoacoustic spectroscopy: Accuracy and resolution," Phys. Med. Biol. **50**, 4409–4428 (2005).
[4] A. Rosencwaig, "Photoacoustic microscopy," Am. Lab. (Shelton, Conn.) **11**, 39–49 (1979).
[5] M. Luukkala and A. Penttinen, "Photoacoustic microscope," Electron. Lett. **15**, 325–326 (1979).
[6] H. Zhang, K. Maslov, G. Stoica, and L. Wang, "Functional photoacoustic microscopy for high-resolution and noninvasive in vivo imaging," Nat. Biotechnol. **24**, 848–851 (2006).
[7] M. Xu and L. V. Wang, "Photoacoustic imaging in biomedicine," Rev. Sci. Instrum. **77**, 041101 (2006).
[8] *Photons Plus Ultrasound: Imaging and Sensing 2005*, edited by A. A.

Oraevsky and L. V. Wang (SPIE, Bellingham, WA, 2005), Vol. 5697.
[9]*Photons Plus Ultrasound: Imaging and Sensing 2006*, edited by A. A. Oraevsky and L. V. Wang (SPIE, Bellingham, WA, 2006), Vol. 6086.
[10]R. A. Kruger, K. D. Miller, H. E. Reynolds, W. L. Kiser, D. R. Reinecke, and G. A. Kruger, "Contrast enhancement of breast cancer in vivo using thermoacoustic CT at 434 MHz—feasibility study," Radiology **216**, 279–283 (2000).
[11]F. F. M. de Mul and C., G. A. Hoelen, "Three-dimensional imaging of blood vessels in tissue using photo-acoustics," J. Vasc. Res. **35**, 192–194 (1998).
[12]X. Wang, Y. Pang, G. Ku, X. Xie, G. Stoica, and L. V. Wang, "Noninvasive laser-induced photoacoustic tomography for structural and functional in vivo imaging of the brain," Nat. Biotechnol. **21**, 803–806 (2003).
[13]R. Kruger, W. Kiser, D. Reinecke, G. Kruger, and K. Miller, "Thermoacoustic molecular imaging of small animals," Mol. Imaging **2**, 113–123 (2003).
[14]S. J. Norton and M. Linzer, "Ultrasonic reflectivity imaging in 3 dimensions—Exact inverse scattering solutions for plane, cylindrical, and spherical apertures," IEEE Trans. Biomed. Eng. **28**, 202–220 (1981).
[15]R. A. Kruger, P. Liu, Y. R. Fang, and C. R. Appledorn, "Photoacoustic ultrasound (PAUS)—reconstruction tomography," Med. Phys. **22**, 1605–1609 (1995).
[16]P. Y. Liu, "The P-transform and photoacoustic image reconstruction," Phys. Med. Biol. **43**, 667–674 (1998).
[17]M. H. Xu, Y. Xu, and L. H. V. Wang, "Time-domain reconstruction-algorithms and numerical simulations for thermoacoustic tomography in various geometries," IEEE Trans. Biomed. Eng. **50**, 1086–1099 (2003).
[18]D. Finch, S. K. Patch, and Rakesh, "Determining a function from its mean values over a family of spheres," SIAM J. Math. Anal. **35**, 1213–1240 (2003).
[19]S. J. Norton and T. Vo-Dinh, "Optoacoustic diffraction tomography: Analysis of algorithms," J. Opt. Soc. Am. A **20**, 1859–1866 (2003).
[20]Y. Xu and L. V. Wang, "Time reversal and its application to tomography with diffracting sources," Phys. Rev. Lett. **92**, 033902 (2004).
[21]M. Xu and L. V. Wang, "Universal back-projection algorithm for photoacoustic computed tomography," Phys. Rev. E **71**, 016706 (2005).
[22]J. Zhang, M. A. Anastasio, X. Pan, and L. V. Wang, "Weighted expectation maximization reconstruction algorithms for thermoacoustic tomography," IEEE Trans. Med. Imaging **24**, 817–820 (2005).
[23]Y. Xu and L. Wang, "Effects of acoustic heterogeneity in breast thermoacoustic tomography," IEEE Trans. Ultrason. Ferroelectr. Freq. Control **50**, 1134–1146 (2003).
[24]J. Zhang and M. A. Anastasio, "Reconstruction of speed-of-sound and electromagnetic absorption distributions in photoacoustic tomography," Proc. SPIE **6086**, 608619 (2006).
[25]M. Frenz, G. Paltauf, and H. Schmidt Kloiber, "Laser-generated cavitation in absorbing liquid induced by acoustic diffraction," Phys. Rev. Lett. **76**, 3546–3549 (1996).
[26]G. Paltauf, H. Schmidt Kloiber, and H. Guss, "Light distribution measurements in absorbing materials by optical detection of laser-induced stress waves," Appl. Phys. Lett. **69**, 1526–1528 (1996).
[27]D.-H. Huang, C.-K. Liao, C.-W. Wei, and P.-C. Li, "Simulations of optoacoustic wave propagation in light-absorbing media using a finite-differnce time-domain method," J. Acoust. Soc. Am. **117**, 2795–2801 (2005).
[28]H. Jiang, Z. Yuan, and X. Gu, "Spatially varying optical and acoustic property reconstruction using finite-element-based photoacoustic tomography," J. Opt. Soc. Am. A **23**, 878–888 (2006).
[29]B. T. Cox and P. C. Beard, "Fast calculation of pulsed photoacoustic fields in fluids using *k*-space methods," J. Acoust. Soc. Am. **117**, 3616–3627 (2005).
[30]B. T. Cox, S. Arridge, K. Köstli, and P. Beard, "Quantitative photoacoustic imaging: Fitting a model of light transport to the initial pressure distribution," Proc. SPIE **5697**, 49–55 (2005).
[31]A. Vogel, J. Noack, G. Hüttman, and G. Paltauf, "Mechanisms of femtosecond laser nanosurgery of cells and tissues," Appl. Phys. B **81**, 1015–1047 (2005).
[32]T. D. Mast, L. P. Souriau, D.-L. D. Liu, M. Tabei, A. I. Nachman, and R. C. Waag, "A *k*-space method for large-scale models of wave propagation in tissue," IEEE Trans. Ultrason. Ferroelectr. Freq. Control **48**, 341–354 (2001).
[33]M. Tabei, T. D. Mast, and R. C. Waag, "A *k*-space method for coupled first-order acoustic propagation equations," J. Acoust. Soc. Am. **111**, 53–63 (2002).
[34]K. Köstli and P. Beard, "Two-dimensional photoacoustic imaging by use of Fourier-transform image reconstruction and a detector with an anisotropic response," Appl. Opt. **42**, 1899–1908 (2003).
[35]B. Fornberg and G. B. Whitham, "A numerical and theoretical study of certain nonlinear wave phenomena," Philos. Trans. R. Soc. London, Ser. A **289**, 373–404 (1978).
[36]N. N. Bojarski, "The *k*-space formulation of the scattering problem in the time domain," J. Acoust. Soc. Am. **72**, 570–584 (1982).
[37]N. N. Bojarski, "The *k*-space formulation of the scattering problem in the time domain: An improved single propagator formulation," J. Acoust. Soc. Am. **77**, 826–831 (1985).
[38]B. Compani-Tabrizi, "K-space scattering formulation of the absorptive full fluid elastic scalar wave equation in the time domain," J. Acoust. Soc. Am. **79**, 901–905 (1986).
[39]Q.-H. Liu, "Generalisation of the *k*-space formulation to elastodynamic scattering problems," J. Acoust. Soc. Am. **97**, 1373–1379 (1995).
[40]G. J. Diebold and T. Sun, "Properties of photoacoustic waves in one-dimension, 2-dimension, and 3-dimension," Acustica **80**, 339–351 (1994).
[41]X. Yuan, D. Borup, J. Wiskin, M. Berggren, and S. A. Johnson, "Simulation of acoustic wave propagation in dispersive media with relaxation losses by using FDTD method with PML absorbing boundary condition," IEEE Trans. Ultrason. Ferroelectr. Freq. Control **46**, 14–23 (1999).
[42]Q.-H. Liu and J. Tao, "The perfectly matched layer (PML) for acoustic waves in absorptive media," J. Acoust. Soc. Am. **102**, 2072–2082 (1997).
[43]Q.-H. Liu, "The Pseudospectral Time Domain (PSTD) algorithm for acoustic waves in absorptive media," IEEE Trans. Ultrason. Ferroelectr. Freq. Control **45**, 1044–1055 (1998).
[44]B. T. Cox and P. C. Beard, "The frequency-dependent directivity of a planar Fabry-Perot polymer film ultrasound sensor," IEEE Trans. Ultrason. Ferroelectr. Freq. Control **54**, 394–404 (2007).